

Multi-gap superconductivity and Shubnikov-de Haas oscillations in single crystals of the layered boride OsB₂

Yogesh Singh,^{1,*} C. Martin,^{1,†} S. L. Bud'ko,¹ A. Ellern,² R. Prozorov,¹ and D. C. Johnston¹

¹*Ames Laboratory and Department of Physics and Astronomy, Iowa State University, Ames, Iowa 50011, USA*

²*Department of Chemistry, Iowa State University, Ames, Iowa 50011, USA*

(Dated: May 29, 2022)

Single crystals of superconducting OsB₂ [$T_c = 2.10(5)$ K] have been grown using a Cu-B eutectic flux. We confirm that OsB₂ crystallizes in the reported orthorhombic structure (space group $Pmmn$) at room temperature. Both the normal and superconducting state properties of the crystals are studied using various techniques. Heat capacity versus temperature $C(T)$ measurements yield the normal state electronic specific heat coefficient $\gamma = 1.95(1)$ mJ/mol K² and the Debye temperature $\Theta_D = 539(2)$ K. The measured frequencies of Shubnikov-de Haas oscillations are in good agreement with those predicted by band structure calculations. Magnetic susceptibility $\chi(T, H)$, electrical resistivity $\rho(T)$ and $C(T, H)$ measurements (H is the magnetic field) demonstrate that OsB₂ is a bulk low- κ [$\kappa(T_c) = 2(1)$] Type-II superconductor that is intermediate between the clean and dirty limits [$\xi(T=0)/\ell = 0.97$] with a small upper critical magnetic field $H_{c2}(T=0) = 186(4)$ Oe. The penetration depth is $\lambda(T=0) = 0.300$ μm . An anomalous (not single-gap BCS) T dependence of λ was fitted by a two-gap model with $\Delta_1(T=0)/k_B T_c = 1.9$ and $\Delta_2(T=0)/k_B T_c = 1.25$, respectively. The discontinuity in the heat capacity at T_c , $\Delta C/\gamma T_c = 1.32$, is smaller than the weak-coupling BCS value of 1.43, consistent with the two-gap nature of the superconductivity in OsB₂. An anomalous increase in ΔC at T_c of unknown origin is found in finite H ; e.g., $\Delta C/\gamma T_c \approx 2.5$ for $H \approx 25$ Oe.

PACS numbers: 74.10.+v, 74.25.Ha, 74.25.Bt, 74.70.Ad

I. INTRODUCTION

Although multigap superconductivity was first addressed theoretically by Suhl *et al.* in 1959,¹ and the first experimental observation of the possible existence of two distinct superconducting gaps was made in 1980 using tunneling measurements on Nb-doped SrTiO₃,² the subject of multigap superconductivity has only recently gained impetus after it was established that several unusual superconducting properties of MgB₂ could be explained within a two-gap superconductivity scenario.^{3,4} There are now several other candidates for multi-gap superconductivity like NbSe₂ (Ref. 5), $R\text{Ni}_2\text{B}_2\text{C}$ ($R = \text{Lu}, \text{Y}$) (Ref. 6), Lu₂Fe₃Si₅ (Refs. 7, 8), and Sr₂RuO₄.⁹

In multigap superconductors distinct superconducting gaps exist on different disconnected parts (sheets) of the Fermi surface (FS) although the interband pairing leads to a single critical temperature T_c .^{1,10} Most superconductors show multi-band conduction, but due to interband pairing the gap has the same magnitude on all bands. When interband pairing is weak then the gaps on different sheets of the FS can have significantly different magnitudes. This can lead to anomalous behavior in the temperature-dependent heat capacity, upper critical magnetic field H_{c2} , and penetration depth λ measurements.^{3,6,11,12}

The compound OsB₂ has a layered crystal structure qualitatively similar to that of MgB₂, except that the B layers are corrugated in OsB₂ instead of flat as in MgB₂.¹³ The crystal structure of OsB₂ is shown in Fig. 1. Figure 1(a) shows the crystal structure of OsB₂ viewed at a slight angle from the b axis. Figure 1(b) shows the structure projected on the ab plane. Along the

c axis the boron layers lie between two planar transition metal layers which are offset along the ab -plane. We have recently reported¹⁴ several anomalous behaviors for polycrystalline samples of the layered superconductor OsB₂ which has a superconducting transition temperature $T_c = 2.1$ K.¹⁵ These unusual behaviors include a reduced specific heat discontinuity at T_c in some samples and a magnetic field penetration depth versus temperature T dependence that was consistent with two-gap superconductivity. We also observed a positive curvature in the T dependence of the upper critical magnetic field H_{c2} . To gain further insights into these interesting behaviors, measurements on single crystals are needed.

Herein we report the growth of OsB₂ single crystals, and structure, isothermal magnetization, dynamic and static magnetic susceptibility, specific heat, electrical resistivity, magnetic field penetration depth, and Shubnikov-de Haas (SdH) oscillation measurements on the crystals to characterize their superconducting and normal state properties. Following a description of the experimental details in Sec. II, the experimental results are given in Sec. III. A summary of the results and our conclusions are given in Sec. IV, including a list in Table IV summarizing the parameters characterizing the physical properties that we obtained.

II. EXPERIMENTAL DETAILS

Single crystals of OsB₂ were grown with a high temperature solution growth method using Cu-B as the flux. First, a polycrystalline sample of OsB₂ was prepared by arc-melting Os powder (99.95%, Alfa Aesar) and B

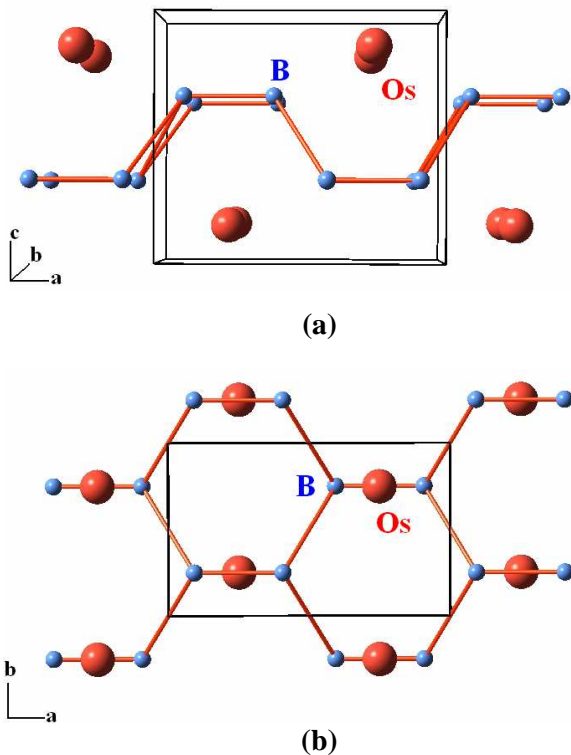


FIG. 1: (Color online) The crystal structure of OsB₂ viewed at a slight angle from the *b* axis. The Os atoms are shown as large (red) spheres while the B atoms are shown as the small (blue) spheres. A single unit cell (shown) contains two formula units. (b) Projection of the OsB₂ structure onto the *ab* plane.

chunks (99.5%, Alfa Aesar) taken in stoichiometric ratio. A Cu-B binary alloy was then prepared at the eutectic composition Cu_{0.87}B_{0.13} by arc-melting. For crystal growth the arc-melted OsB₂ sample (~ 0.5 g) was placed in a 2 mL Al₂O₃ crucible. About 5 g Cu-B flux was placed on top of the OsB₂ ingot. The crucible with a lid was placed in a vertical tube furnace which was then evacuated and purged with high purity Ar gas repeatedly (≈ 10 times) after which the growth was started in a flow (≈ 60 cc/min) of Ar. The furnace was heated to 800 °C in 30 min, then heated to 1450 °C in 6 hrs and held at this temperature for 6 hrs. The furnace was then cooled to 1020 °C at a rate of 2 °C/hr and then rapidly cooled to room temperature. Well-formed crystals with flat facets were obtained after the Cu-B flux had been dissolved in dilute nitric (HNO₃) acid. A scanning electron micrograph of a typical crystal is shown in Fig. 2(a).

Some single crystals were crushed for powder X-ray diffraction (XRD) measurements. The XRD patterns were obtained using a Rigaku Geigerflex diffractometer with Cu K α radiation, in the 2θ range from 10 to 90° with a 0.02° step size. Intensity data were accumulated for 5 s per step.

For single crystal structure determination, a well-

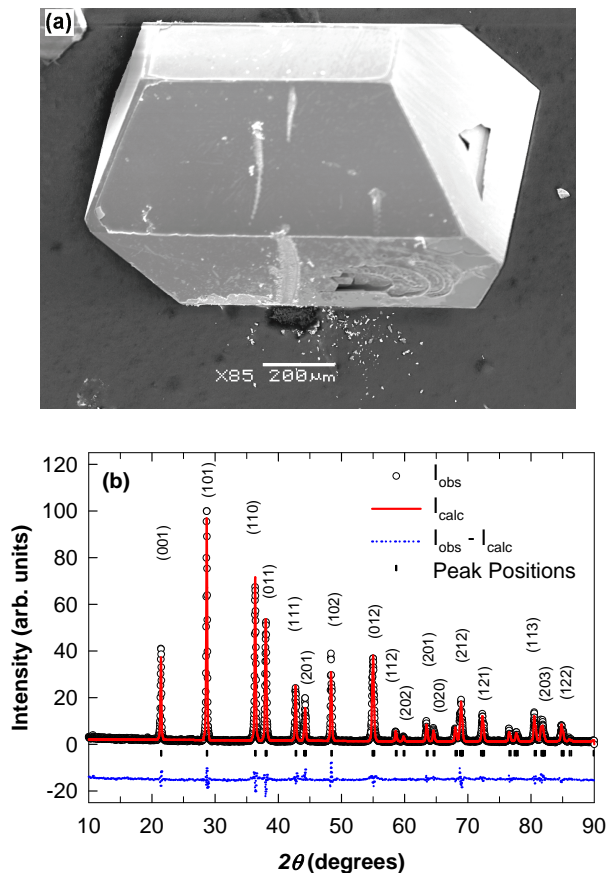


FIG. 2: (Color online) (a) Scanning electron microscope image of a typical OsB₂ crystal. (b) Rietveld refinement of the powder X-ray diffraction data of crushed OsB₂ crystals. The open black circles represent the observed X-ray pattern, the solid red line represents the fitted pattern, the dotted blue line represents the difference between the observed and calculated intensities and the vertical black bars represent the peak positions.

shaped crystal ($0.27 \times 0.18 \times 0.15$ mm³) was selected. The data collection for the crystal was performed using a Bruker Apex II instrument with Cu K α radiation at $T = 100$ K and was solved with latest version of the Apex software package which is reliable for a combination of numerical and multi-scan absorption correction. The initial cell constants were obtained from three series of ω scans at different starting angles. Each series consisted of 30 frames collected at intervals of 0.3° in a 10° range about ω with the exposure time of 5 s per frame. The obtained reflections were successfully indexed by an automated indexing routine built in the Apex program. The final cell constants were calculated from a set of strong reflections from the actual data collection. The data were collected using the full sphere routine by collecting 20 sets of frames with 1 degree scans in ω with an exposure time of 5 s per frame. This data set was corrected for Lorentz and polarization effects. The absorption correction was a combination of a numerical one based on

TABLE I: Crystal data and structure refinement of OsB₂. Here $R1 = \sum ||F_{\text{obs}}| - |F_{\text{calc}}|| / \sum |F_{\text{obs}}|$ and $wR2 = (\sum [w(|F_{\text{obs}}|^2 - |F_{\text{calc}}|^2)^2] / \sum [w(|F_{\text{obs}}|^2)^2])^{1/2}$, where F_{obs} is the observed structure factor and F_{calc} is the calculated structure factor.

| | |
|--------------------------------------|---|
| Temperature | 100(2) K |
| Crystal system, space group | Orthorhombic, $Pm\bar{m}n$ |
| Unit cell parameters | $a = 4.6729(3)$ Å, $b = 2.8702(2)$ Å, $c = 4.0792(3)$ Å |
| Unit cell volume | $54.711(7)$ Å ³ |
| Z (formula units per unit cell) | 2 |
| Molar volume | $16.474(2)$ cm ³ /mol |
| Density (calculated) | 12.858 Mg/m ³ |
| Absorption coefficient | 212.327 mm ⁻¹ |
| F(000) | 172 |
| Data / restraints / parameters | 65 / 12 / 12 |
| Goodness-of-fit on F^2 | 1.015 |
| Final R indices [$I > 2\sigma(I)$] | $R1 = 0.0294$ $wR2 = 0.0736$ |
| Extinction coefficient | $0.016(3)$ |

a face indexing and an additional correction based on fitting a function to the empirical transmission surface as sampled by multiple equivalent measurements¹⁶ using the Apex software.¹⁷

The temperature dependences of the dc magnetic susceptibility and isothermal magnetization were measured using a commercial Superconducting Quantum Interference Device (SQUID) magnetometer (MPMS5, Quantum Design). The resistivity and heat capacity were measured using a commercial Physical Property Measurement System (PPMS, Quantum Design). The resistivity was measured using a four-probe technique with a current of 5 mA along the b axis. The dynamic susceptibility was measured between 0.5 K and 2.6 K using a 10 MHz tunnel-diode driven oscillator (TDO) circuit with a volume susceptibility sensitivity $\Delta\chi \approx 10^{-8}$.¹⁸ The details of the measurement and the extraction of magnetic susceptibility and penetration depth from TDO measurements have been described in our previous work.¹⁴

III. RESULTS

A. Crystal Structure of OsB₂

The powder XRD pattern for crushed single crystals of OsB₂ is shown in Fig. 2(b). All the lines in the X-ray pattern could be indexed to the known orthorhombic $Pm\bar{m}n$ (No. 59) structure and a Rietveld refinement¹⁹ of the X-ray pattern, shown in Fig. 2(b), gave the lattice parameters $a = 4.6855(6)$ Å, $b = 2.8730(3)$ Å and $c = 4.0778(4)$ Å. These values are in very good agreement

TABLE II: Atomic coordinates and anisotropic displacement parameters for OsB₂ in space group $Pm\bar{m}n$ (second setting). The Os atoms occupy Wyckoff $2a$ ($\frac{1}{4}, \frac{1}{4}, z$) positions and the B atoms occupy $4f$ ($x, \frac{1}{4}, z$) positions. U_{11} , U_{22} and U_{33} are the anisotropic thermal parameters in units of Å² defined within the thermal parameter of the intensity as $e^{-2\pi^2(h^2 a^2 U_{11} + k^2 b^2 U_{22} + l^2 c^2 U_{33})}$.

| atom | x | y | z | U_{11} | U_{22} | U_{33} |
|------|----------|-----|-----------|----------|----------|----------|
| Os | 1/4 | 1/4 | 0.1527(2) | 0.003(1) | 0.004(1) | 0.003(1) |
| B | 0.049(6) | 1/4 | 0.359(4) | 0.004(8) | 0.001(8) | 0.006(8) |

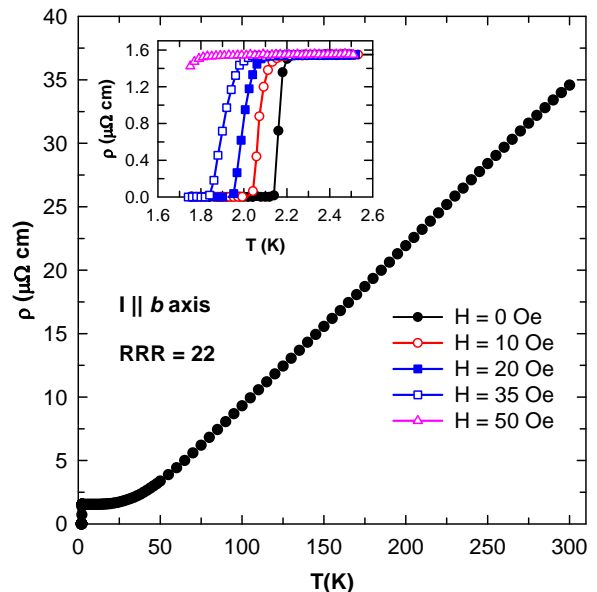


FIG. 3: (Color online) Electrical resistivity ρ for a single crystal of OsB₂ versus temperature T with current $I = 5$ mA along the b axis and with applied magnetic field $H = 0$ Oe. The inset shows the $\rho(T)$ data between $T = 1.7$ and 2.6 K measured in various applied magnetic fields H as indicated.

with our previously reported values [$a = 4.6851(6)$ Å, $b = 2.8734(4)$ Å, and $c = 4.0771(5)$ Å] for a polycrystalline sample.¹⁴

Single crystal XRD data were obtained at $T = 100$ K. The systematic extinctions of peaks in the XRD data were consistent with the space group $Pm\bar{m}n$,¹⁷ in agreement with earlier reports from single crystal and powder XRD measurements on OsB₂.²⁰ The positions of the atoms were found by direct methods and were refined in full-matrix anisotropic approximation. Some parameters obtained from the single crystal structure refinement are given in Table I and the final atomic positions and anisotropic thermal parameters are given in Table II.

B. Electrical Resistivity

The electrical resistivity ρ versus T of a single crystal of OsB₂ from 1.75 K to 300 K measured in zero applied magnetic field H and with a current $I = 5$ mA applied along the b axis, is shown in Fig. 3. The $\rho(T)$ shows metallic behavior with an approximately linear decrease in resistivity on cooling from room temperature to 50 K. This behavior is similar to that observed earlier for a polycrystalline sample.¹⁴ At low temperatures ρ becomes only weakly temperature dependent and reaches a residual resistivity $\rho_0 = 1.55 \mu\Omega \text{ cm}$ just above 2.2 K as seen in the inset of Fig. 3. The large residual resistivity ratio $\text{RRR} = \rho(300 \text{ K})/\rho_0 = 22$ indicates a well crystallized sample.

The inset of Fig. 3 shows the low T data measured in various H . The ρ in $H = 0$ drops abruptly below 2.20 K and reaches zero by 2.14 K, as highlighted in the inset of Fig. 3. This superconducting transition was observed earlier by us for a polycrystalline sample,¹⁴ consistent with the original report in 1975 of superconductivity in OsB₂ by Vandenberg et al.¹⁵ As expected, the superconducting transition shifts to lower T with increasing H . These data were used to determine the upper critical magnetic field $H_{c2}(T)$ which will be discussed later. In particular, for each applied field H , this H is taken to be H_{c2} for the temperature at which the resistance drops to zero.

C. Isothermal Magnetization and Magnetic Susceptibility

1. Normal State

The isothermal magnetization M versus H applied along the b axis is shown in Fig. 4(a) at various T . At high $T > 100$ K, M is diamagnetic and proportional to H with a slope that is almost constant between $T = 100$ and $T = 300$ K. At lower T , M initially increases with H towards a positive value before showing saturation at a field of about 500 Oe. For higher H , M turns over and becomes diamagnetic. For $H > 1$ T, M is linear in H with a nonzero y -intercept. A similar $M(H)$ behavior is also observed in measurements with H applied along the a and c axes and is consistent with the presence of a small amount of paramagnetic and/or ferromagnetic impurities in the sample. Contributions from paramagnetic impurities are also observed at low temperatures in our normal state magnetic susceptibility χ measurements via a Curie-Weiss-like upturn in Fig. 5 below. The $M(H)$ data indicate that the impurity contribution saturates at high H . We extract the saturation magnetization $M_S(T)$ by fitting the $M(H, T)$ by the expression $M(H, T) = M_S(T) + \chi_{\text{int}}H$, where χ_{int} is the intrinsic susceptibility. The $M_S(T)$ data so obtained are shown in Fig. 4(b).

The normal state $\chi \equiv M/H$ versus T for OsB₂, measured between 1.8 K and 300 K with $H = 3$ T applied

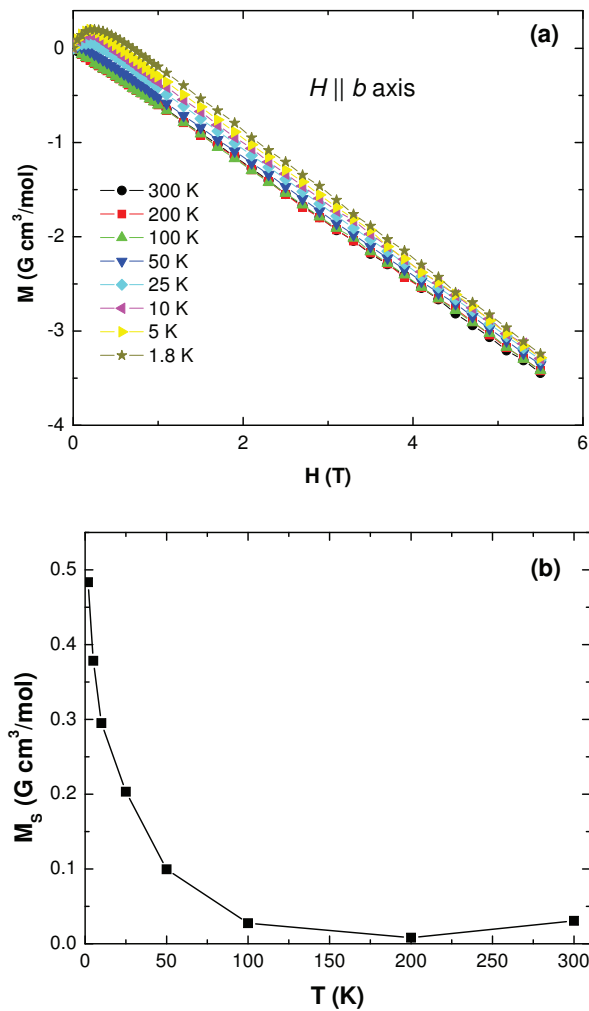


FIG. 4: (Color online) (a) Isothermal magnetization M versus magnetic field H at various temperatures T with H applied along the b axis. (b) Saturation magnetization M_S versus T obtained by fitting the $M(H)$ data above $H = 2$ T at various T by the expression $M(H, T) = M_S(T) + \chi(T)H$.

along the a , b , and c axes, is shown in Fig. 5. The powder average susceptibility $\chi(T)$ and the $\chi(T)$ for a polycrystalline sample from Ref. 14 are also shown in Fig. 5. The $\chi(T)$ for single crystalline OsB₂ is weakly temperature dependent between 50 K and 300 K. The upturn at low temperatures is most likely due to the presence of small amounts of paramagnetic impurities as mentioned above. The solid curve through the powder average $\chi(T)$ data is a fit by the expression $\chi(T) = \chi_{\text{int}} + \frac{C}{T-\theta}$. The fit gave the values $\chi_{\text{int}} = -4.56(3) \times 10^{-5} \text{ cm}^3/\text{mol}$, $C = 1.43(1) \times 10^{-4} \text{ cm}^3 \text{ K}/\text{mol}$, and $\theta = -12.1(5)$ K. This value of C is equivalent to about 0.04 mol% of spin-1/2 impurities with a g -factor $g = 2$. The large negative value of θ is probably due, at least in part, to saturation of the paramagnetic impurities by the relatively high 3 T field. The powder average value at 300 K is $\bar{\chi}(300 \text{ K}) = -4.50 \times 10^{-5} \text{ cm}^3/\text{mol}$. A diamagnetic susceptibility for a transition metal compound is rare, but not

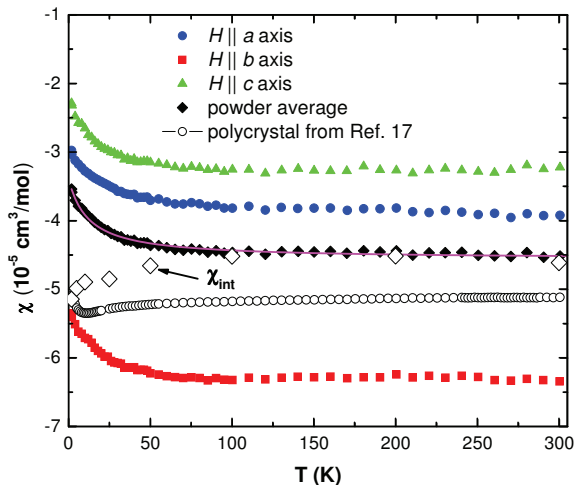


FIG. 5: (Color online) Magnetic susceptibility χ versus temperature T for a single crystal of OsB_2 with a magnetic field $H = 3$ T applied along the a , b , and c axes. The powder average $\chi(T)$ and the $\chi(T)$ for a polycrystalline sample (from Ref. 14) are also shown. The solid curve through the powder average $\chi(T)$ data is a fit by the expression $\chi(T) = \chi_{\text{int}} + \frac{C}{T-\theta}$. The intrinsic susceptibility obtained by correcting the powder averaged $\chi(T)$ for the ferromagnetic impurity contribution $M_S(T)$, $\chi_{\text{int}}(T) = \chi(T) - M_S(T)/H$ is shown as open diamond symbols.

unprecedented.¹⁴

Fig. 5 also shows the intrinsic susceptibility $\chi_{\text{int}}(T)$ obtained by correcting the powder averaged susceptibility for the presence of ferromagnetic and/or paramagnetic impurities as discussed above. Here we have assumed that $M_S(T)$ is isotropic so that we can use the $M_S(T)$ data obtained from $M(H, T)$ data for the b axis to correct the powder averaged susceptibility.

The χ along different crystallographic directions is anisotropic with the value (averaged between $T = 100$ K and 300 K) along the b axis ($\approx -6.25 \times 10^{-5} \text{ cm}^3/\text{mol}$) being much smaller than the susceptibility along the a ($\approx -3.75 \times 10^{-5} \text{ cm}^3/\text{mol}$) or c ($\approx -3.25 \times 10^{-5} \text{ cm}^3/\text{mol}$) axes which are quite similar. The similarity of the χ values along the a and c axes is surprising given the layered nature of the crystal structure which is built up of alternating Os and B layers in the a - b plane that are stacked along the c axis. However, theoretical Fermi surface (FS) calculations have shown that there are quasi-one-dimensional tubular structures running along the b axis, and the FSs along the a and c axes are quite similar.²¹

As described in Ref. 14, one can estimate the paramagnetic Pauli spin susceptibility χ_P from the intrinsic susceptibility χ_{int} according to

$$\chi_{\text{int}} = \chi_{\text{orb}} + \chi_P, \quad (1)$$

where χ_{orb} is the total orbital susceptibility, which includes the diamagnetic core contribution, the paramagnetic Van Vleck contribution, and the Landau diamagnetic contribution from the conduction electrons. In

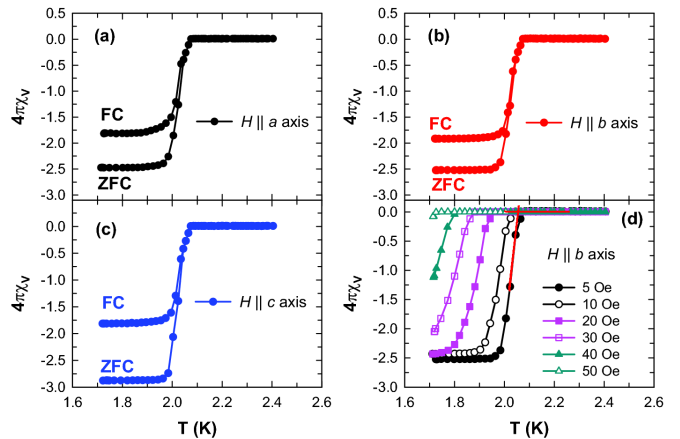


FIG. 6: (Color online) Temperature T dependence of the zero-field-cooled (ZFC) and field-cooled (FC) dimensionless volume susceptibility $4\pi\chi_v$ in terms of the superconducting volume fraction ($4\pi\chi_v$) of a single crystal of OsB_2 with a magnetic field $H = 5$ Oe applied along the (a) a axis, (b) b axis, and (c) c axis. (d) The T dependence of the ZFC superconducting volume fraction $4\pi\chi_v$ of a single crystal of OsB_2 measured in various magnetic fields H applied along the b axis. The construction used to determine $T_c(H)$ is illustrated by the red straight line for $H = 5$ Oe. At low T , the $4\pi\chi_v$ values are all more negative than -1 due to demagnetization effects.

Ref. 14, we estimated $\chi_{\text{orb}} = -7.8 \times 10^{-5} \text{ cm}^3/\text{mol}$. However, the accuracy of this estimate for χ_{orb} is unknown (see also below). Using this value of χ_{orb} , our measured $\bar{\chi}_{\text{int}}(300 \text{ K}) = -4.50 \times 10^{-5} \text{ cm}^3/\text{mol}$ and Eq. (1), for our single crystalline OsB_2 we obtain a powder average $\chi_P = 3.23 \times 10^{-5} \text{ cm}^3/\text{mol}$.

From χ_P one can estimate the density of states at the Fermi level $N(\epsilon_F)$ for both spin directions using the relation²²

$$\chi_P = \mu_B^2 N(\epsilon_F) = \left(3.233 \times 10^{-5} \frac{\text{cm}^3}{\text{mol}} \right) N(\epsilon_F), \quad (2)$$

where μ_B is the Bohr magneton and the equality on the far right-hand side is for $N(\epsilon_F)$ in units of states/(eV f.u.) for both spin directions, where “f.u.” means “formula unit.” Taking the above average value of χ_P for OsB_2 , we get $N(\epsilon_F) = 1.00(3)$ states/(eV f.u.) for both spin directions. This value is a factor of two larger than the value from our specific heat measurements below as well as from band structure calculations [$N(\epsilon_F) = 0.55$ states/(eV f.u.)],²³ indicating that our estimate of the orbital susceptibility above is too negative. Using Eq. (2) and the band structure density of states value gives the revised estimate $\chi_P = 1.8 \times 10^{-5} \text{ cm}^3/\text{mol}$. Then using the measured $\bar{\chi}_{\text{int}}(300 \text{ K})$ and Eq. (1) yields a revised powder averaged orbital susceptibility $\chi_{\text{orb}} = -6.3 \times 10^{-5} \text{ cm}^3/\text{mol}$.

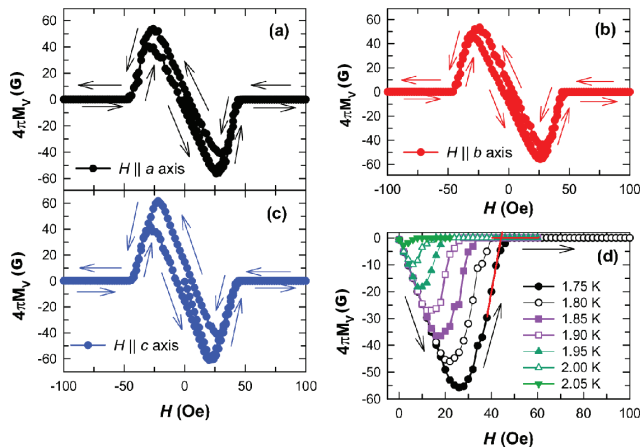


FIG. 7: (Color online) Hysteresis loops at 1.7 K of the volume magnetization $M_v(H)$ normalized by $1/4\pi$, versus applied magnetic field H applied along the (a) a axis, (b) b axis, and (c) c axis. The arrows next to the data indicate the direction of field ramping during the measurement. (d) Normalized magnetization $M_v(H)$ at various temperatures T versus H along the b axis. The construction used to determine $H_{c2}(T)$ is shown by the solid red line for $T = 1.75$ K.

2. Superconducting State

The temperature dependence of the anisotropic zero-field-cooled (ZFC) and field-cooled (FC) dimensionless dc volume magnetic susceptibility χ_v of a single crystal of OsB_2 measured from 1.7 to 2.5 K is plotted in Figs. 6(a), (b), and (c) in a field of 5 Oe parallel to the a , b and c axes, respectively, where $\chi_v = M_v/H$ and M_v is the volume magnetization. Complete diamagnetism in the absence of demagnetization effects corresponds to $\chi_v = -1/4\pi$, so the data have been normalized by $1/4\pi$. A sharp diamagnetic drop in the susceptibility along all three directions, below $T_c = 2.05$ K, signals the transition into the superconducting state. The large Meissner fraction seen in the FC data for all three directions indicates weak magnetic flux pinning in the crystal. The data have not been corrected for the demagnetization factors N_α ($\alpha = a, b, c$) which give $-4\pi\chi_v = \frac{1}{1-N_\alpha}$ for the respective measured value. From the ZFC data at the lowest temperatures in Fig. 6, one obtains $N_a = 0.60$, $N_b = 0.60$ and $N_c = 0.65$, yielding $N_a + N_b + N_c = 1.85$. This sum is greater than the value of unity expected for an ellipsoid of revolution. The reason for this discrepancy is not known.

In Fig. 6(d) the temperature dependences of χ_v measured with various H applied along the b axis are shown. As expected the superconducting transition is suppressed to lower temperatures with increasing H . From these $\chi_v(H)$ data the critical field $H_{c2}(T)$ has been estimated using the construction in Fig. 6(d), illustrated for $H = 5$ Oe. The $H_{c2}(T)$ has been determined by fitting a straight line to the data for a given field in the superconducting state just below T_c and to the data in the

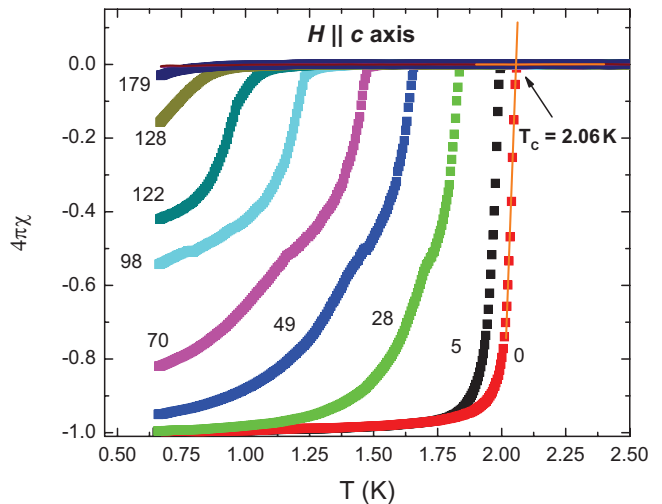


FIG. 8: (Color online) Dynamic susceptibility χ normalized by $1/4\pi$, versus temperature T at a frequency of 10 MHz with various applied magnetic fields H in units of Oe. The $4\pi\chi$ data have been normalized to a minimum value of -1 at the lowest T . The construction used to determine $T_c(H)$ is shown by the red line for $H = 0$.

normal state above T_c and taking the temperature at which these lines intersect as the T_c at that H .

The hysteretic volume magnetization M_v normalized by $1/4\pi$ versus H loops measured at $T = 1.7$ K with H applied along the a , b , and c axes are shown in Figs. 7(a), (b), and (c), respectively. There is a large reversible part in all the M_v data recorded with increasing and decreasing H which again indicates very weak magnetic flux pinning in the material. The $M_v(H)$ data recorded at various fixed T with H applied along the b axis are shown in Fig. 7(d). Similar data (not shown) with H along the a and c axes were also recorded. The initial slope of the $M_v(H)$ curves is larger than the value -1 expected for perfect diamagnetism, which indicates a nonzero demagnetization factor, consistent with the $4\pi\chi_v(T)$ data in Fig. 6. From the $M_v(H)$ curves in Fig. 7(d) we estimated the critical field $H_{c2}(T)$ from the construction illustrated in Fig. 7(d) for $T = 1.75$ K.

The dynamic ac susceptibility $\chi(T)$ measured between 0.6 K and 2.5 K at a frequency of 10 MHz in various H is shown in Fig. 8. To determine $H_{c2}(T)$ from the data in Fig. 8 we fitted a straight line to the data in the normal state and to the data just below T_c for a given applied magnetic field and took the value of the T at which these lines intersect as the $T_c(H)$. This construction is shown in Fig. 8 for the data at $H = 0$. By inverting $T_c(H)$ we obtain $H_{c2}(T)$. The H_{c2} has also been obtained in a similar way from the $\chi(T) \equiv M(T)/H$ SQUID magnetometer data (not shown here) between 1.7 K and 2.4 K in various applied magnetic fields.

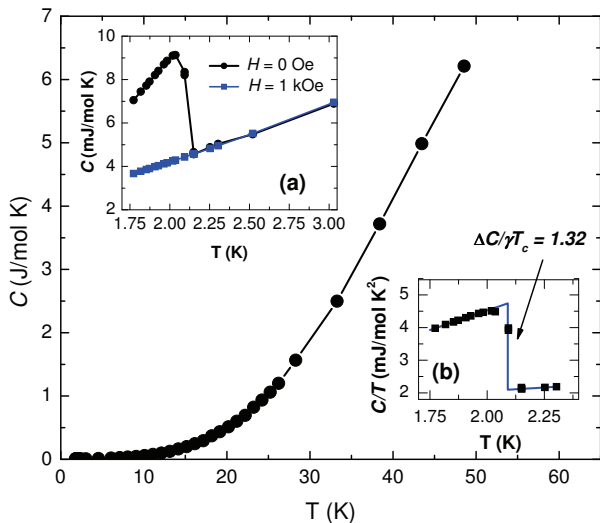


FIG. 9: Heat capacity C versus temperature T of a single crystal of OsB_2 between 1.75 K and 48 K measured in zero magnetic field H . Inset (a) shows the $C(T)$ data between 1.75 K and 3 K measured with $H = 0$ and $H = 1$ kOe applied along the c axis. Inset (b) shows the data for $H = 0$ plotted as $C(T)/T$ versus T between $T = 1.75$ and 2.5 K. The solid curve in inset (b) is a construction to estimate the heat capacity jump ΔC at T_c .

D. Heat Capacity

Figure 9 shows the heat capacity C versus T data measured on a single crystal of OsB_2 . The main panel shows the $C(T)$ data measured in $H = 0$ between $T = 1.75$ K and 48 K. The data below $T = 10$ K could be fitted by the expression $C/T = \gamma + \beta T^2$ where the first term is the contribution from the conduction electrons and the second term is the contribution from the lattice. The fit (not shown) gave the values $\gamma = 1.95(1)$ mJ/mol K^2 and $\beta = 0.0372(3)$ mJ/mol K^4 . From the value of β one can estimate the Debye temperature θ_D using the expression²²

$$\Theta_D = \left(\frac{12\pi^4 R n}{5\beta} \right)^{1/3} = \left[(1.944 \times 10^6) \frac{n}{\beta} \right]^{1/3}, \quad (3)$$

where R is the molar gas constant, n is the number of atoms per formula unit ($n = 3$ for OsB_2), and the equality on the far right-hand side is for Θ_D in K and β in mJ/mol K^4 . We obtain $\Theta_D = 539(2)$ K for OsB_2 . The values of γ , β , and θ_D obtained above are in very good agreement with the values we reported previously for an unannealed polycrystalline sample.¹⁴

The $C(T)$ data below $T = 3$ K measured in zero and 1 kOe applied field are shown in inset (a) of Fig. 9. A sharp step-like anomaly at $T = 2.1$ K is observed in the $H = 0$ Oe data and confirms the bulk nature of the superconductivity in single crystal OsB_2 . The anomaly is suppressed to below $T = 1.75$ K in a field of $H = 1$ kOe.

The inset (b) shows the $H = 0$ Oe heat capacity plotted as $C(T)/T$ versus T between $T = 1.75$ and 2.5 K. The jump in the specific heat ΔC at the superconducting transition T_c is usually normalized as $\Delta C/\gamma T_c$. From the construction shown as the solid curve through the data in Fig. 9 inset (b) we obtain $\Delta C/\gamma T_c = 1.32$. This value is smaller than the weak-coupling BCS value 1.43.³⁰ Considering the sharp anomaly observed at T_c it is unlikely that the smaller value of $\Delta C/\gamma T_c$ arises from a distribution of T_c 's due to inhomogeneties in the sample. We suggest that the small value of $\Delta C/\gamma T_c$ arises from the multi-gap nature of the superconductivity as evidenced from our penetration depth measurements discussed later.

The electron-phonon coupling constant λ_{ep} can be estimated in the single-gap superconductivity approximation using McMillan's formula²⁴ which relates the superconducting transition temperature T_c to λ_{ep} , the Debye temperature Θ_D , and the Coulomb repulsion constant μ^* ,

$$T_c = \frac{\Theta_D}{1.45} \exp \left[-\frac{1.04(1 + \lambda_{\text{ep}})}{\lambda_{\text{ep}} - \mu^*(1 + 0.62\lambda_{\text{ep}})} \right], \quad (4)$$

which can be inverted to give λ_{ep} in terms of T_c , Θ_D and μ^* as

$$\lambda_{\text{ep}} = \frac{1.04 + \mu^* \ln\left(\frac{\Theta_D}{1.45T_c}\right)}{(1 - 0.62\mu^*) \ln\left(\frac{\Theta_D}{1.45T_c}\right) - 1.04}. \quad (5)$$

From the value $\Theta_D = 539$ K obtained above from heat capacity measurements, and using $T_c = 2.1$ K we get $\lambda_{\text{ep}} = 0.41$ and 0.50 for $\mu^* = 0.10$ and 0.15, respectively. These values of λ_{ep} are similar to those found for polycrystalline samples and suggest that OsB_2 is a moderate-coupling superconductor.¹⁴

The density of states at the Fermi energy $N(\epsilon_F)$ for both spin directions can be estimated from the values of γ and λ_{ep} using the relation²²

$$\gamma = \gamma_0(1 + \lambda_{\text{ep}}). \quad (6)$$

where

$$\gamma_0 = \frac{\pi^2 k_B^2}{3} N(\epsilon_F) = 2.359 N(\epsilon_F), \quad (7)$$

k_B is Boltzmann's constant and the equality on the right-hand side of Eq. (7) is for γ_0 in mJ/mol K^2 and $N(\epsilon_F)$ in states/(eV f.u.) for both spin directions. Using the above $\gamma = 1.95$ mJ/(mol K^2), we find $N(\epsilon_F) = 0.59$ and 0.55 states/(eV f.u.) for the above $\lambda_{\text{ep}} = 0.41$ and 0.50, respectively. These values are in excellent agreement with the value from band structure calculations [$N(\epsilon_F) = 0.55$ states/(eV f.u.) for both spin directions].²³ This agreement indicates that OsB_2 is a weakly correlated electron system, consistent with the

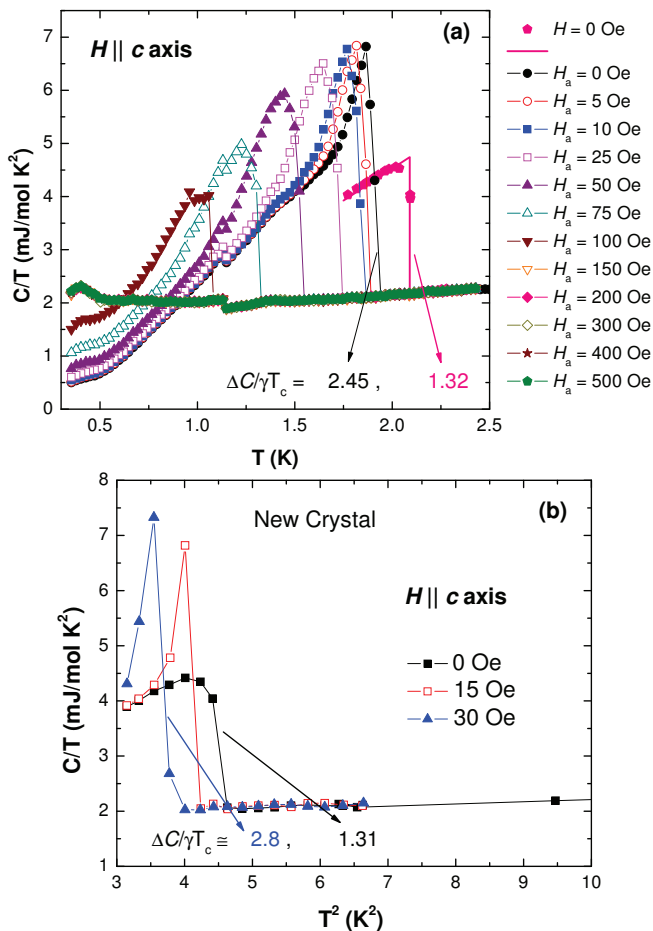


FIG. 10: (Color online) (a) Heat capacity C divided by temperature T versus T of a single crystal of OsB_2 in various applied magnetic fields H_a . A remanent magnetic field $H \approx 25$ Oe was present over the nominal value of the applied field H_a listed in the figure legend. The true $H = 0$ Oe data from Fig. 9 inset (b) are also included for comparison. (b) C/T versus T^2 measured in various true magnetic fields H for a different OsB_2 crystal.

observed diamagnetic susceptibility in Fig. 5(b) above. Henceforth we will take the bare density of states to be

$$N(\epsilon_F) = 0.55 \text{ states}/(\text{eV f.u.}) \quad (8)$$

for both spin directions, which corresponds to $\mu^* = 0.15$ and $\lambda_{\text{ep}} = 0.50$.

To obtain the critical magnetic field versus temperature we have measured $C(T)$ in various H . Figure 10(a) shows the $C(T)/T$ versus T data between $T = 0.3$ K and 2.5 K, measured in various applied magnetic fields H_a . A remanent field of about 25 Oe was present in addition to the applied magnetic field H_a in these measurements. For comparison the true $H = 0$ Oe data from Fig. 9 inset (b) are also shown. The superconducting transition seen as an abrupt jump in $C(T)/T$ is suppressed to lower T with increasing H_a as expected. However, the magnitude $\Delta C/\gamma T_c$ of the anomaly at T_c is initially larger

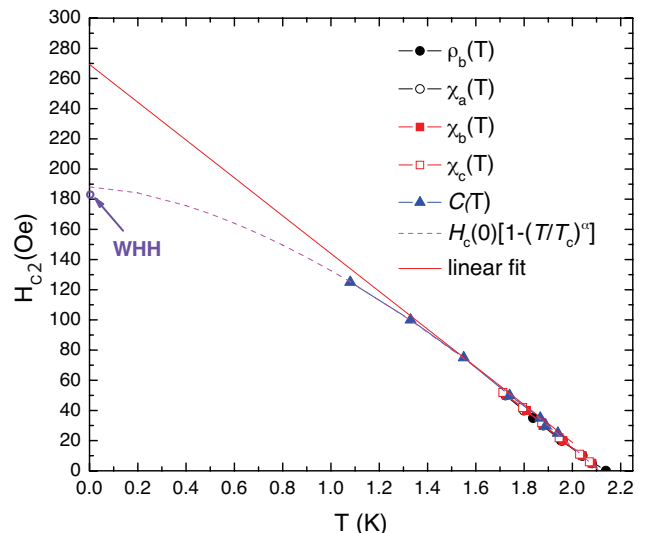


FIG. 11: (Color online) Upper critical magnetic field H_{c2} versus temperature T extracted from different types of measurements, as indicated. The straight line is a linear fit to the data near T_c . The dashed curve is a fit by the expression $H_{c2}(T) = H_{c2}(0)[1 - (T/T_c)^\alpha]$. The circle at $T = 0$ K labeled "WHH" is the estimate of $H_{c2}(T = 0)$ using the WHH formula in the clean limit (see text).

than that observed in zero magnetic field. As shown by the arrows in Fig. 10(a), $\Delta C/\gamma T_c$ increases from 1.32 for $H = 0$ Oe to 2.45 for $H_a = 0$ Oe (which is close to $H = 25$ Oe) suggesting a divergent nature of C at T_c in an applied magnetic field.

The superconducting anomaly moves to lower T with increasing H and is not observed above $H_a = 100$ Oe ($H \approx 125$ Oe). The step in all data at about $T = 1.15$ K arises from a problem in the measurement and is not intrinsic to the sample.

To further study the enhanced ΔC anomaly in low fields we measured $C(T)$ for another single crystal in various (true) H . The data are plotted as $C(T)/T$ versus T^2 in Fig. 10(b). We again observe that the anomaly at the superconducting transition becomes first order-like in a finite field showing that this feature is intrinsic to single crystalline OsB_2 .

This $\Delta C(H)$ behavior is similar to that recently observed for $T_2\text{Ga}_9$ ($T = \text{Rh}$ and Ir),^{25,26} and for single crystals of ZrB_{12} ,²⁷ where it was suggested that the Type-I superconductivity in these materials led to the superconducting transition in a finite magnetic field to be first order-like, resulting in a divergent $\Delta C(H)$ at T_c . A similar divergent $\Delta C(H)$ at T_c was observed 75 years ago for the Type-I superconductor thallium.²⁸ The $C(T, H)$ behavior observed for single crystal OsB_2 in Figs. 10(a) and (b) is similar to that observed for the materials mentioned above and might suggest that OsB_2 is a Type-I superconductor. However, our estimates of the Ginzburg-Landau parameter $\kappa = 2(1)$ below indicate that OsB_2 is a small- κ Type-II superconductor. The unusual features in the $C(T, H)$ for OsB_2 are therefore not understood at

present but might be related to the multi-gap nature of the superconductivity.

E. Upper Critical Magnetic Field $H_{c2}(T)$

The $H_{c2}(T)$ data obtained from all of the above measurements are plotted in Fig. 11. In the temperature range of the SQUID magnetometer measurements (1.7 K to 2.4 K) all the data match well and the temperature dependence of H_{c2} is linear (solid curve extrapolated to $T = 0$ K in Fig. 11) with the slope $\frac{dH_c}{dT} = -125$ Oe/K. This linear slope can be used to get an estimate of the $T = 0$ K upper critical field using the WHH formula for the clean limit $H_{c2}(0) = -0.693 T_c (\frac{dH_c}{dT}|_{T_c})$.²⁹ Using the above value of $\frac{dH_c}{dT}|_{T_c} = -125$ Oe/K and $T_c = 2.10$ K we get $H_{c2}(0) = 182$ Oe.

The $H_{c2}(T)$ data at the lower temperatures $T \sim 1$ K in Fig. 11 show a deviation from linearity with a negative curvature. To obtain another estimate of $H_{c2}(0)$, the $H_{c2}(T)$ data in the whole T range were fitted by the empirical power law expression $H_{c2}(T) = H_{c2}(0) \left[1 - (\frac{T}{T_c})^\alpha\right]$ with $H_{c2}(0)$ and α as fitting parameters and with fixed $T_c = 2.15$ K. The fit shown as the dashed curve in Fig. 11 gave the values $H_{c2}(0) = 188(2)$ Oe and $\alpha = 1.55(3)$. This estimate of $H_{c2}(0)$ is close to the value of 182 Oe obtained above using the WHH formula. These two fits together yield our final value $H_{c2}(0) = 186(4)$ Oe. From Fig. 11 it can also be seen that there is negligible anisotropy in the measured $H_{c2}(T)$ from $T = 1.7$ to 2.4 K.

For a Type-II superconductor near T_c , the superconducting coherence length ξ can be estimated from the measured H_{c2} using the Ginzburg-Landau relation³⁰

$$H_{c2} = \frac{\phi_0}{2\pi\xi^2}, \quad (9)$$

where $\phi_0 = hc/2e = 2.068 \times 10^{-7}$ G cm² is the flux quantum. We obtain an estimate of ξ using instead the zero-temperature value $H_{c2}(T = 0) = 186(4)$ Oe arrived at above to obtain $\xi(T = 0) = 0.133(2)$ μm .

F. Superfluid Density

The measured magnetic penetration depth $\lambda(T)$ in the superconducting state is related to the so-called London penetration depth $\lambda_L(T)$ by³⁰

$$\lambda(T) \approx \lambda_L(T) \sqrt{1 + \frac{\xi_0(T)}{\ell(T)}}, \quad (10)$$

where

$$\xi_0 = \frac{\hbar v_F}{\pi \Delta(0)} \quad (11)$$

is the BCS coherence length, ℓ is the quasiparticle mean free path and v_F is the Fermi velocity. Including the influence of ℓ gives the modified coherence length ξ as³⁰

$$\frac{1}{\xi} = \frac{1}{\xi_0} + \frac{1}{\ell}. \quad (12)$$

The limit $\xi/\ell \rightarrow 0$ is called the clean limit and the opposite limit the dirty limit.

The superfluid density $\rho_s(T)$ is related to $\lambda(T)$ by³⁰

$$\rho_s(T) = \frac{m^* c^2}{4\pi e^2 \lambda^2(T)}, \quad (13)$$

where m^* is the effective mass of the individual quasiparticles, c is the speed of light in vacuum, e is the elementary charge and ρ_s is the density of quasiparticles that have condensed into the superconducting state, not the density of Cooper pairs which is a factor of two smaller. The normalized ratio of $\rho_s(T)$ to $\rho_s(0)$ is simply

$$\frac{\rho_s(T)}{\rho_s(0)} = \frac{\lambda^2(0)}{\lambda^2(T)}. \quad (14)$$

We now estimate whether OsB₂ is in the clean or dirty limit or somewhere in between, by estimating the ratio $\xi(0)/\ell$. The value of $\xi(0)$ was derived in the preceding section. We will estimate the mean-free-path ℓ using the measured resistivity at low temperatures and the $N(\epsilon_F)$ in Eq. (8). First, the conductivity σ is written as²²

$$\sigma = \frac{ne^2\tau}{m^*} \quad (15)$$

where n is the conduction carrier density and τ is the mean-free scattering time of the current carriers. We then express $\tau = v_F/\ell$, and from Eq. (15) we get

$$\ell = \frac{\hbar m^* v_F \sigma}{e^2 \hbar n}, \quad (16)$$

where in SI units the first term on the right is $\hbar/e^2 = 4108 \Omega$. Next we write both v_F and n in terms of the known $N(\epsilon_F)$ and then substitute these expressions into Eq. (16).

The (average) Fermi velocity has not been reported from band calculations. Therefore we calculate both v_F and n from $N(\epsilon_F)$ by assuming a three-dimensional single-band model with a spherical Fermi surface, yielding²²

$$v_F = \frac{\pi^2 \hbar^3}{2m_e^2 (m^*/m_e)^2} \mathcal{D}(\epsilon_F), \quad (17)$$

$$n = \frac{\pi^4}{3} \left[\frac{\hbar^2}{2m^*} \mathcal{D}(\epsilon_F) \right]^3, \quad (18)$$

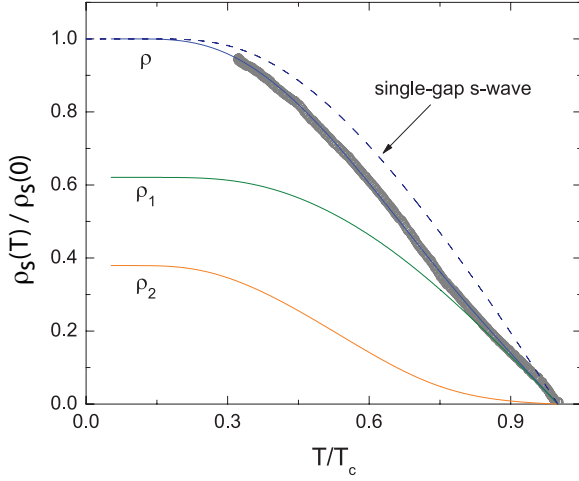


FIG. 12: (Color online) The normalized superfluid density $\rho_s(T)/\rho_s(0)$ versus reduced temperature T/T_c . The solid curve through the data is a fit by the two-gap γ model for superconductivity. The curves ρ_1 and ρ_2 are the individual contributions from the two gaps.

where $\mathcal{D}(\epsilon_F)$ is the density of states at the Fermi energy in units of states/(erg cm³) for both spin directions. Substituting Eqs. (17) and (18) into (16), and using $\rho = 1/\sigma$, gives

$$\ell = \frac{\hbar}{e^2} \frac{3(m^*/m_e)^2}{\pi^2 \left[\frac{\hbar^2}{2m_e} \mathcal{D}(\epsilon_F) \right]^2} \rho, \quad (19)$$

where m_e is the free-electron mass. The expression converting $\mathcal{D}(\epsilon_F)$ in units of states/(erg cm³) to the conventional units of states/(eV f.u.) for both spin directions appropriate to the above definition of $N(\epsilon_F)$ is

$$\mathcal{D}(\epsilon_F) = N(\epsilon_F) \left[\frac{1}{\text{eV f.u.}} \right] \left(\frac{1 \text{ eV}}{1.6022 \times 10^{-12} \text{ erg}} \right) \frac{N_A}{V_M}, \quad (20)$$

where N_A is Avogadro's number and V_M is the molar volume. Substituting Eq. (20) into (19) and putting in the values of the constants gives

$$\ell = 2.372 \times 10^{-14} \frac{(m^*/m_e)^2 V_M^2}{N^2(\epsilon_F) \rho}, \quad (21)$$

$$v_F = 2.622 \times 10^9 \frac{N(\epsilon_F)}{(m^*/m_e)^2 V_M} \quad (22)$$

where ℓ is in cm, v_F is in cm/s, $N(\epsilon_F)$ is in states/(eV f.u.) for both spin directions, V_M is in cm³/mol and ρ is in Ω cm.

Inserting $V_M = 16.47$ cm³/mol from Table I, $m^*/m_e = 1$ (see Sec. III H below), $N(\epsilon_F) = 0.55$ states/(eV f.u.) for both spin directions from our heat capacity data above,

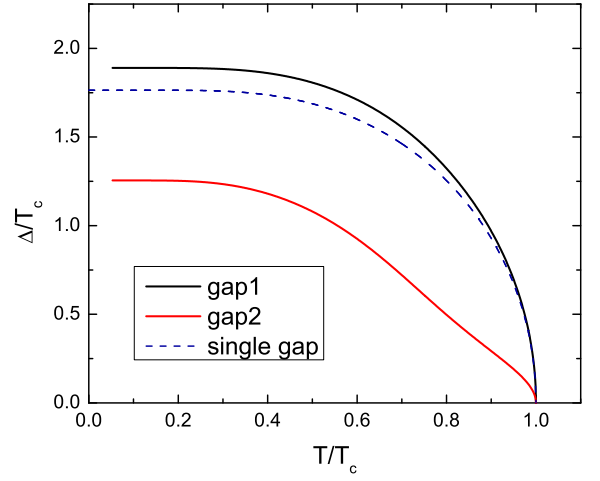


FIG. 13: (Color online) Temperature T dependence of the two gaps Δ_1 (top black solid curve) and Δ_2 (bottom red solid curve). Also shown by the blue dashed curve is the BCS prediction for a single gap.

and $\rho = 1.55 \times 10^{-6} \Omega$ cm at 2.25 K from Fig. 3 into Eq. (21) gives $\ell = 0.137 \mu\text{m}$ at 2.25 K. Then using $\xi(0) = 0.133 \mu\text{m}$ from above gives $\xi(0)/\ell(0) = 0.97$. Therefore OsB₂ is in neither the clean limit nor the dirty limit, but in between. Irrespective of this difficulty, we will assume the clean limit in order to be able to carry out calculations for comparison with our measured penetration depth data. From Eq. (22) we also obtain $v_F = 8.75 \times 10^7$ cm/s.

The $\rho_s(T)/\rho_s(0)$ versus T/T_c calculated from the $\lambda(T)$ data using Eq. (14) is shown in Fig. 12. The dashed curve is the T dependence of ρ_s expected for a BCS single-gap s -wave superconductor. It is clear that our $\rho_s(T)$ shows marked deviations from the single-gap BCS curve. This is consistent with our previous observations for polycrystalline samples.¹⁴ The solid curve through the data is a fit by a two-gap γ model.³⁴ From the fit we obtained $\lambda(T \rightarrow 0) = 0.300 \mu\text{m}$.

The partial superfluid densities $\rho_1(T)$ and $\rho_2(T)$ from the fit to the two-gap model are shown as solid curves in Fig. 12. The T dependences of the two gaps are shown in Fig. 13 plotted as normalized gaps $\Delta/k_B T_c$ versus the reduced temperature T/T_c . For comparison, the T dependence of a single s -wave BCS gap is shown as the dashed curve. The $T = 0$ value of the two gaps are $\Delta_1(0) = 1.88 k_B T_c$ and $\Delta_2(0) = 1.25 k_B T_c$, respectively. The ratios of these two gaps to the single BCS gap value $\Delta_{\text{BCS}}(0) = 1.76 k_B T_c$ are $\Delta_1(0)/\Delta_{\text{BCS}}(0) = 1.07$ and $\Delta_2(0)/\Delta_{\text{BCS}}(0) = 0.71$. The values of these two gaps agree by construction with the theorem that in a two-gap superconductor, one of the gaps will always be larger than the BCS gap, whereas the second will always be smaller.¹⁰ This constraint is a built-in result of the self-consistent solution to the two-gap γ model.

G. Additional Superconducting Parameters

The zero-temperature thermodynamic critical field $H_c(0)$ of a superconductor is related to the zero-temperature superconducting gap $\Delta(0)$ in a single-gap BCS model by the expression³⁰

$$\frac{H_c(0)^2}{8\pi} = \frac{\mathcal{D}(\epsilon_F)\Delta(0)^2}{4}, \quad (23)$$

where, as above, $\mathcal{D}(\epsilon_F)$ is the density of states at the Fermi energy for both spin directions in units of states/(erg cm³). We use this expression as an approximation to our two-gap model to obtain a value of $H_c(0)$. Using the density of states value $N(\epsilon_F) = 0.55$ states/eV f.u. for both spin directions from the above heat capacity measurements and Eq. (20) gives $\mathcal{D}(\epsilon_F) = 1.26 \times 10^{34}$ states/(erg cm³). Using the larger gap found from fitting the penetration depth data and $\Delta(0)/k_B T_c = 1.88$ which gives $\Delta(0) = 5.45 \times 10^{-16}$ erg, Eq. (23) yields $H_c(0) = 153$ Oe. We can now derive the Ginzburg-Landau parameter κ using the above $H_{c2}(0) = 186$ Oe via³⁰

$$\kappa = \frac{H_{c2}}{\sqrt{2}H_c} = 0.86. \quad (24)$$

This value is marginally on the Type-II side of the value $\kappa = 1/\sqrt{2} \approx 0.707$ separating Type-I from Type-II superconductivity, thus justifying the above notation of the measured critical field as being the upper critical field H_{c2} instead of the thermodynamic critical field H_c .

Another estimate of κ can be obtained using the relation³³

$$\kappa(T) = \frac{\kappa(0)}{[1 + (T/T_c)^2]} = 2^{1/2} \frac{2\pi H_c(0)\lambda(0)^2}{\phi_0[1 + (T/T_c)^2]}, \quad (25)$$

where $\kappa(0)$, $H_c(0)$, and $\lambda(0)$ are the $T = 0$ values of the Ginzburg-Landau parameter, the thermodynamic critical field, and penetration depth respectively. With the value $H_c(0) = 153$ Oe obtained above and the value $\lambda(0) = 0.300 \mu\text{m}$, we get $\kappa(0) = 6.0$ and $\kappa(T_c) = 3.0$.

Two more estimates of $\kappa(T_c)$ can be made using the relations³⁰

$$\kappa(T_c) = 0.96 \frac{\lambda_L(0)}{\xi(0)}, \quad (\text{clean limit}) \quad (26)$$

$$\kappa(T_c) = 0.715 \frac{\lambda_L(0)}{\ell}. \quad (\text{dirty limit}) \quad (27)$$

Using $\lambda(0) = 0.300 \mu\text{m}$, $\xi(0) = 0.133 \mu\text{m}$, $\ell(T > T_c) = 0.137 \mu\text{m}$ and Eq. (10), one obtains $\kappa(T_c) = 2.17$ and 0.78 from Eqs. (26) and (27), respectively.

The above four estimates of $\kappa(T_c)$ are all greater than $1/\sqrt{2}$ and therefore all indicate that single crystalline OsB₂ is a small- κ Type-II superconductor with $\kappa(T_c) = 2(1)$.

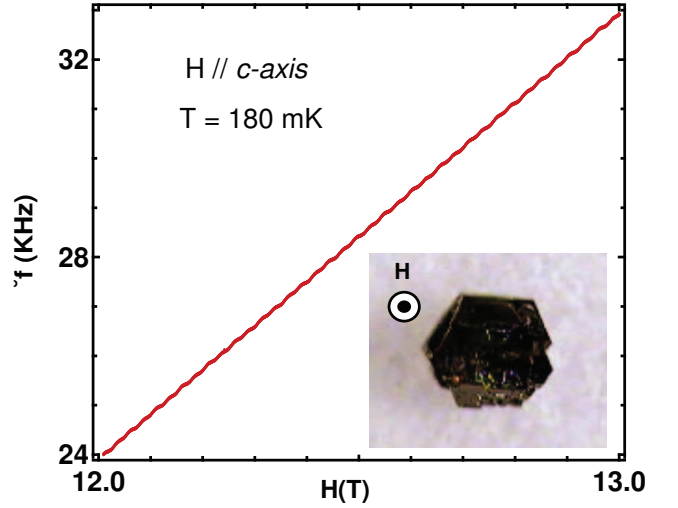


FIG. 14: (Color online) The change $\Delta f = f(H) - f(0)$ in the tunnel diode oscillator (TDO) frequency f versus magnetic field H measured at $T = 180$ mK with H applied along the c axis. The inset shows an image of the crystal used for the measurement. The c axis is out of the plane of the image.

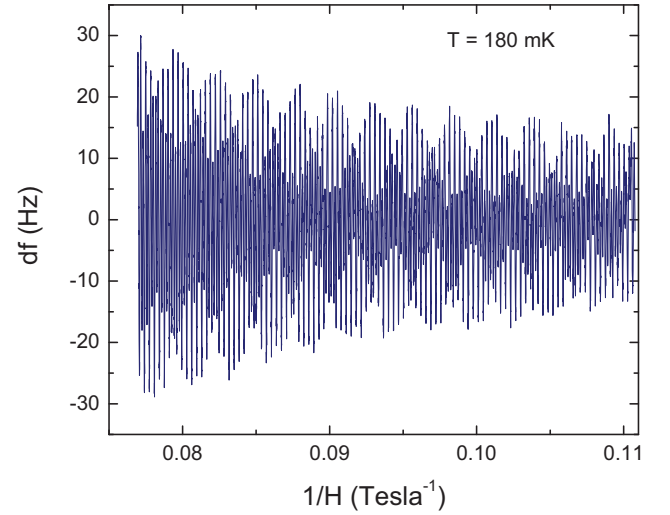


FIG. 15: (Color online) The oscillating part of the TDO frequency $df = \Delta f - \text{smooth background}$, versus the reciprocal of the magnetic field $1/H$ for H applied along the c axis.

H. Shubnikov-de Haas (SdH) Oscillations

Shubnikov-de Haas (SdH) oscillations in $\rho(H)$ were observed as oscillations in the skin depth, which in turn were obtained from the oscillation frequency shift versus H of a tunnel diode oscillator (TDO) in which the sample is placed inside the inductor of the LC circuit. Oscillations were observed for $T = 0.12$ – 3.3 K in magnetic fields up to $H = 14$ T. Since $H_{c2}(0) = 186$ Oe from Sec. III E, such fields quench the superconductivity and the measurements are therefore in the normal state. The inset of Fig. 14 shows an image of the crystal and the direction

TABLE III: Experimental (expt) and theoretical²¹ (thy) Shubnikov-de Haas frequencies F for single crystal OsB₂ with the magnetic field applied along the c axis and in the ab plane, where n is the harmonic number. Also included are values for the effective mass m^*/m_e and the electron-phonon coupling constant λ_{ep} of the electrons in specific orbits. For the data with $H \parallel ab$ plane, the field was oriented about 15° from the b axis, and hence the measured frequencies are not in general equal to the theoretical values for $H \parallel b$.

| F | n | F_{expt} (T) | F_{thy} (T) | $\frac{m^*}{m_e}$ expt | $\frac{m^*}{m_e}$ thy | λ_{ep} expt |
|------------------------------------|-----|--------------------------|-------------------------|---------------------------|--------------------------|------------------------|
| H \parallel c | | | | | | |
| F_1 | 1 | 2767 | 3023 | 1.03(4) | 1.05 | ≈ 0 |
| F_1 | 2 | 5528 | — | — | — | — |
| F_2 | 1 | 5905 | 5902 | 0.81(3) | 0.50 | 0.63(5) |
| F_2 | 2 | 11 806 | — | — | — | — |
| F_3 | | 660 | | | | |
| H \parallel ab | | | | | | |
| F_1 | | 745 | | | | |
| F_2 | | 932 | | | | |
| F_3 | | 2983 | ~ 2177 | | | |
| F_4 | | 3812 | ~ 3265 | 0.87 | 0.95 | ≈ 0 |
| F_5 | | 3957 | ~ 3888 | 1.13 | 0.92 | 0.23 |
| F_6 | | 5138 | 5115 | 0.92 | 0.62 | 0.48 |
| F_7 | 1? | 5697 | ~ 5291 | | | |
| F_8 | | 6153 | 6189 | 0.96 | 0.45 | 1.13 |
| F_9 | 2? | 11 311 | | | | |

of the applied field $H \parallel c$ axis where the c axis points out of the plane of the figure.

The shift $\Delta f = f(H) - f(0)$ in the TDO frequency versus H applied along the c axis measured at $T = 0.18$ K is shown versus H in Fig. 14. Small oscillations can be seen riding on a smooth background. This H -dependent background is due to the tunnel diode circuit that is partially exposed to the applied field. The oscillations are more clearly visible when a smooth background is subtracted from $\Delta f(H)$ using a non-oscillating piecewise cubic hermite interpolating polynomial algorithm in Matlab. Figure 15 shows the resulting oscillating part of the TDO frequency shift df versus the inverse magnetic field $1/H$ where df is the frequency shift after the background subtraction.

To get the frequencies of the SdH oscillations at each T , a power spectrum was obtained by taking a Fourier transformation of the oscillation data such as in Fig. 15. The resulting power spectra obtained for the measurements at $T = 0.12$ – 3.3 K are shown in Fig. 16. The data reveal two clear fundamental frequencies $F_1 = 2767$ T and $F_2 = 5905$ T and possibly a third $F_3 = 660$ T as marked in the plot in Fig. 16, although the intensity of the line at F_3 is much weaker than the intensities of the prominent sharp lines at F_1 and F_2 . We also observe the second harmonics for F_1 and F_2 but none for F_3 , as

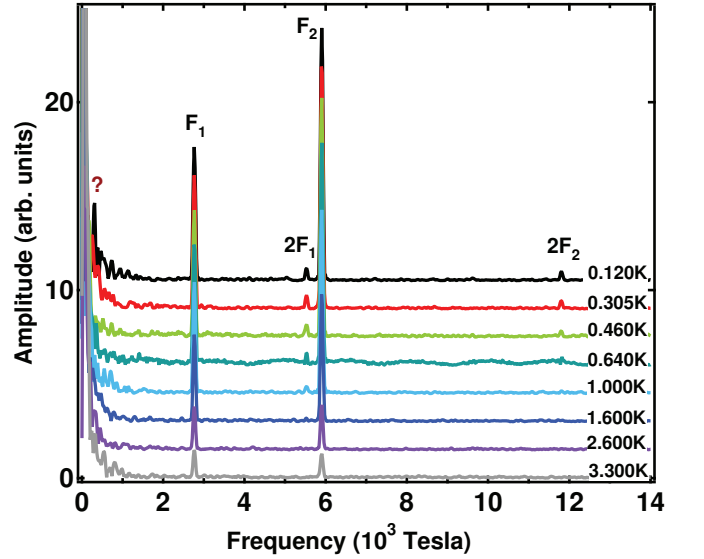


FIG. 16: (Color online) Power spectra of Shubnikov-de Haas oscillations obtained at the indicated temperatures from Fourier transformation of the quantum SdH oscillation data such as in Fig. 15 at the indicated temperatures. The spectra are shifted vertically by arbitrary amounts for clarity of presentation.

shown in Fig. 16 and listed in Table III.

Recent first principles calculations of the Fermi surface (FS) showed three bands at the Fermi level, consisting of two nested deformed ellipsoidal surfaces (first and second bands) and a corrugated tubular surface (third band) along the b axis.²¹ For a magnetic field applied along the c axis, the two closed electronic orbits which give rise to SdH oscillations are the cross-sectional areas of the two deformed ellipsoids normal to the applied field. The theoretically predicted frequencies of oscillations are 3023 and 5902 T.²¹ These values are in reasonable agreement with the experimentally observed frequencies $F_1 = 2767$ and $F_2 = 5905$ T of the SdH oscillations for OsB₂ for measurements with $H \parallel c$ axis. Since the frequencies of the SdH oscillations are inversely proportional to the area of the respective electronic orbits, we can assign the F_1 oscillations as coming from the smaller inner ellipsoid while the F_2 oscillations can be assigned to the outer ellipsoid. For the third tubular band, there are no closed orbits for $H \parallel c$ axis. The origin of the third frequency F_3 in Fig. 16 is therefore not understood at present.

The T dependences of the amplitudes $A(T)$ of oscillation in Fig. 16 can be used to estimate the respective effective masses for the bands responsible for the oscillations. The normalized $A(T)$ is given by the Lifshitz-Kosevich formula^{31,32}

$$A(T) = \frac{X}{\sinh X}, \quad \text{where } X = \pi^2 \left(\frac{m^*}{m_e} \right) \left(\frac{k_B T}{\mu_B B} \right), \quad (28)$$

and $B \approx H$ is the magnetic induction. The dimensionless variable X is proportional to the product of the ef-

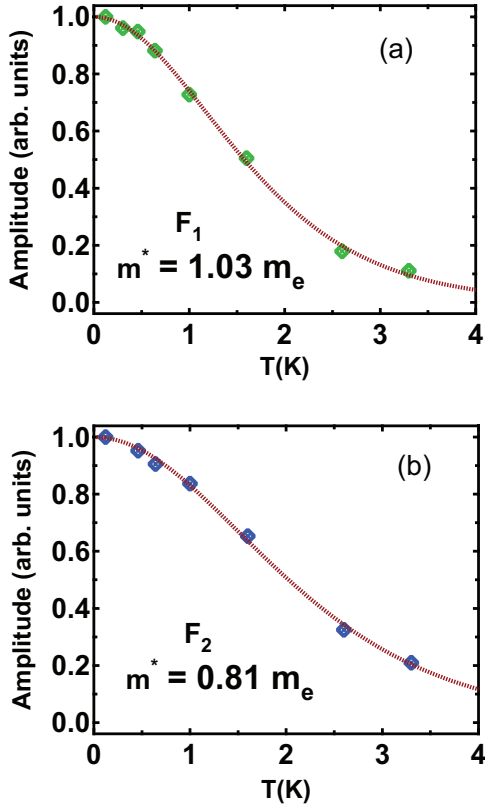


FIG. 17: (Color online) (a) and (b) Fits to the amplitude versus T data for the peaks F_1 and F_2 respectively, by Eq. (28). The values of the respective effective masses m^* for the two Fermi surface extrema are indicated in the figures.

effective mass and the ratio of the thermal to magnetic energies. Therefore, by fitting the T -dependent amplitudes of the peaks in the power spectra in Fig. 16 by Eq. (28) one can obtain the m^* values for the Fermi surface electrons responsible for the respective oscillations. Figures 17(a) and (b) show $A(T)$ for the F_1 and F_2 peaks, respectively. The fits by Eq. (28) are also shown as solid curves through the data. We obtain $m_1^* = 1.03(4)m_e$ for F_1 and $m_2^* = 0.81(3)m_e$ for F_2 . The band masses predicted by theory for these two orbits are $m_{b1} = 1.05m_e$ and $m_{b2} = 0.50m_e$, respectively.²¹ The electron-phonon coupling constant λ_{ep} can be estimated by using the expression $m^* = (1 + \lambda_{ep})m_b$. Using the above values of m^* and m_b we obtain $\lambda_{ep} \approx 0$ for F_1 and $\lambda_{ep} = 0.63(5)$ for F_2 .

Figure 18 shows the power spectra for quantum oscillations measurements performed with H applied perpendicular to the c axis. Due to the shape of our crystal we were only able to perform measurements with H tilted about 15 degrees away from the b axis as shown in the inset of Fig. 18. The power spectra reveal nine different frequencies which are labeled in Fig. 18 and their values are given in Table III.

For $H||b$ axis, theory predicts at least six frequencies for quantum oscillations, two coming from the deformed

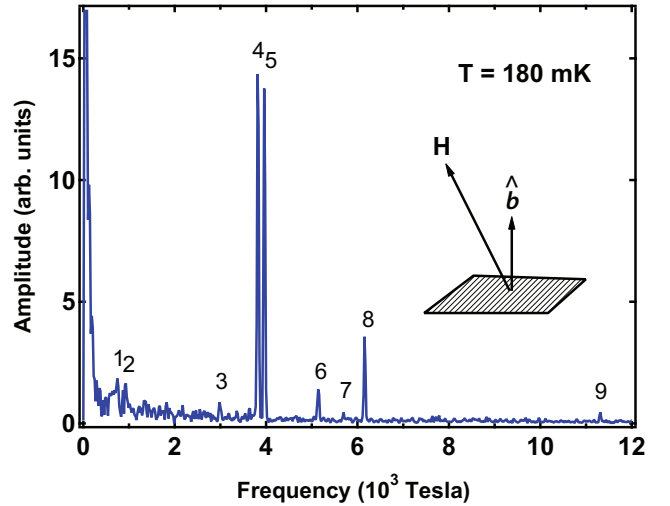


FIG. 18: (Color online) Power spectra of Shubnikov-de Haas oscillations obtained at temperatures $T = 180$ mK for H about 15° away from the b -axis in the ab -plane (see inset), obtained from Fourier transformation of quantum oscillation data (not shown) similar to those in Fig. 15. The indices i for the quantum SdH oscillation frequencies F_i are as indicated. These frequencies are listed in Table III.

ellipsoidal Fermi surfaces, and four from different closed orbits on the tubular Fermi surface as shown in Fig. 3 in Ref. 21. For the two deformed ellipsoidal FS sheets, it was predicted that the frequencies of oscillation would vary linearly with angle as the field H is moved from $H || b$ axis toward $H || c$ axis.²¹ Thus, for the first deformed ellipsoid the frequency of oscillation should change at a rate of about -25 T/degree and for the second deformed ellipsoid it should change at a rate of about -3.8 T/degree as one moves away from $H || b$ axis.²¹ The predicted values of the frequencies of oscillation for $H || b$ axis are 5490 T and 6246 T, respectively, for the two deformed ellipsoids. If we use the above rates of change of the frequencies and the fact that we measured with H about 15 degrees away from the b axis, then the expected frequencies are 5115 T and 6189 T, respectively, as listed in Table III. These values are close to the observed frequencies F_6 and F_8 , respectively. Therefore, we can assign the frequencies F_6 and F_8 as coming from the two deformed ellipsoidal FS sheets. The assignment of the other frequencies in Table III is difficult since the angular dependence of frequencies arising from the tubular FS sheet is not known. We note that frequencies F_1 and F_2 in Fig. 18 are much smaller and F_9 is almost a factor of 2 larger than any of the four frequencies predicted for the tubular FS sheet.²¹ We suggest that F_9 is most likely a second harmonic of F_7 . The remaining 4 frequencies $F_3 = 2983$ T, $F_4 = 3812$ T, $F_5 = 3957$ T, and $F_7 = 5697$ T can be compared to the theoretically predicted frequencies 2177 T, 3265 T, 3888 T, and 5291 T.²¹ The experimentally observed frequencies are similar to those predicted considering the unknown angular dependence of the frequencies

arising from the tubular FS sheet. Thus we can tentatively assign these observed frequencies to the quasi-two-dimensional tubular FS sheet.

The most intense frequencies in Fig. 18, F_4 , F_5 , F_6 , and F_8 , were used to estimate the effective masses by fitting the T dependences of these frequencies by Eq. (28). We obtain $m_4^* = 0.87m_e$, $m_5^* = 1.13m_e$, $m_6^* = 0.92m_e$, and $m_8^* = 0.96m_e$. The corresponding theoretically predicted band masses are $m_{b4} = 0.95m_e$, $m_{b5} = 0.92m_e$, $m_{b6} = 0.62m_e$, and $m_{b8} = 0.45m_e$. Using the expression $m^* = (1 + \lambda_{ep})m_b$, we estimate electron-phonon interaction constants $\lambda_4 \approx 0$, $\lambda_5 \approx 0.23$, $\lambda_6 \approx 0.48$, and $\lambda_8 \approx 1.13$. It should be noted that the frequencies F_6 and F_8 arise from the deformed ellipsoidal FS sheets. Thus, we find that λ_{ep} is larger for the ellipsoidal FS sheets compared to the quasi-two-dimensional tubular FS sheet. This suggests that the superconductivity in OsB₂ is driven by the two deformed ellipsoidal FS sheets. The average value of λ_{ep} estimated above from McMillan's formula Eq. (5) was 0.4–0.5 which agrees with our inference that λ_{ep} is small on some FS sheets and is larger on others.

The above experimental and theoretical SdH data are summarized in Table III.

IV. SUMMARY AND CONCLUSIONS

We have grown high quality single crystals of OsB₂ using a novel Cu-B eutectic flux. Measurements on these crystals confirm bulk superconductivity. The crystallographic parameters of a single crystal are described above in Tables I and II and Fermi surface properties in Table III. The various parameters describing other normal and superconducting state properties are summarized here in Table IV.

The heat capacity measurements show some unusual behaviors. The zero field anomaly at the superconducting transition $\Delta C/\gamma T_c \approx 1.3$ is smaller than the weak-coupling BCS value of 1.43. We suggest that this arises due to the two-gap nature of the superconductivity in OsB₂. The occurrence of two superconducting gaps is supported by the anomalous temperature dependence of the penetration depth which could be fitted by the new γ model for multi-gap superconductors³⁴ with the magnitudes of the two gaps being $\Delta_1(T=0)/k_B T_c = 1.90$ and $\Delta_2(T=0)/k_B T_c = 1.25$, respectively. The zero-temperature upper critical field was determined to be $H_{c2}(0) = 186$ Oe. Four estimates of the Ginzburg-Landau parameter gave $\kappa(T_c) \sim 1-3$ and thus indicate that OsB₂ is a small- κ Type-II superconductor. We observed an anomalous increase in the heat capacity jump at T_c measured in a finite magnetic field H . For example, at $H \approx 25$ Oe, $\Delta C/\gamma T_c \approx 2.5$. This anomalous increase in $\Delta C/\gamma T_c$ was confirmed for two batches of crystals.

The high quality of the crystals made it possible for us to study the anisotropy of the Fermi surface (FS) of OsB₂ by measuring Shubnikov-de Haas quantum oscilla-

TABLE IV: Parameters describing the physical properties of OsB₂. The symbols are superconducting transition temperature T_c , electrical resistivity ρ_b along the b axis, estimated mean-free path along the b axis just above T_c , $\ell_b(2.25$ K), normal state magnetic susceptibility χ_α ($\alpha = a, b, c$) and powder average $\bar{\chi}$ measured in $H = 3$ T, linear specific heat coefficient γ , Debye temperature Θ_D , electron-phonon coupling constant λ_{ep} , bare band structure density of states derived from heat capacity measurements $N(\epsilon_F)$ for both spin directions, Fermi velocity v_F , nearly isotropic upper critical magnetic field H_{c2} , superconducting coherence length ξ , magnetic penetration depth λ , thermodynamic critical field H_c , and Ginzburg-Landau parameter κ .

| Quantity | value |
|---------------------|---|
| T_c | 2.10(5) K |
| $\rho_b(2.25$ K) | 1.55 $\mu\Omega$ cm |
| $\ell_b(2.25$ K) | 0.137 μm |
| $\chi_a(300$ K) | -3.9×10^{-5} cm ³ /mol |
| $\chi_b(300$ K) | -6.3×10^{-5} cm ³ /mol |
| $\chi_c(300$ K) | -3.2×10^{-5} cm ³ /mol |
| $\bar{\chi}(300$ K) | -4.50×10^{-5} cm ³ /mol |
| γ | 1.95(1) mJ/mol K ² |
| Θ_D | 539(2) K |
| λ_{ep} | 0.50 |
| $N(\epsilon_F)$ | 0.55 states/(eV f.u.) |
| v_F | 9.1×10^7 cm/s |
| $H_{c2}(T=0)$ | 186(4) Oe |
| $\xi(T=0)$ | 0.133(2) μm |
| $\lambda(T=0)$ | 0.300 μm |
| $H_c(T=0)$ | 153 Oe |
| $\kappa(T_c)$ | 2(1) |

tions via contactless rf skin depth measurements. Some experimentally observed frequencies could be assigned to those predicted theoretically. The effective masses estimated for the two deformed ellipsoidal FS sheets are larger than the predicted band masses and suggest a large electron-phonon coupling constant $\lambda_{ep} \sim 0.5-1$ for these FS sheets. A much smaller value of λ_{ep} was found for the third quasi-two-dimensional tubular FS sheet. These results suggest that the superconductivity in OsB₂ is driven by the two ellipsoidal FS sheets. This would also explain the negligible anisotropy in the measured upper critical fields between the three crystallographic directions.

Acknowledgments

Work at the Ames Laboratory was supported by the Department of Energy-Basic Energy Sciences under Contract No. DE-AC02-07CH11358. R.P. also acknowledges support from NSF Grant number DMR-05-53285 and from the Alfred P. Sloan Foundation.

- * Present address: I. Physikalisches Institut, Georg-August-Universität Göttingen, D-37077, Göttingen, Germany
- † Present address: Department of Physics, B2126 New Physics Building, University of Florida, Gainesville, Florida 32611, USA
- [1] H. Suhl, B. T. Matthias, L. T. Walker, *Phys. Rev. Lett.* **3**, 552 (1959).
- [2] G. Binnig, A. Baratoff, H. E. Hoenig, and J. G. Bednorz, *Phys. Rev. Lett.* **45**, 1352 (1980).
- [3] F. Bouquet, R. A. Fisher, N. E. Phillips, D. G. Hinks, and J. D. Jorgensen, *Phys. Rev. Lett.* **87**, 047001 (2001).
- [4] H. J. Choi, D. Roundy, H. Sun, M. L. Cohen, and S. G. Louie, *Nature* **418**, 758 (2002).
- [5] E. Boaknin, M. A. Tanatar, J. Paglione, D. Hawthorn, F. Ronning, R. W. Hill, M. Sutherland, L. Taillefer, J. Sonier, S. M. Hayden, and J.W. Brill, *Phys. Rev. Lett.* **90**, 117003 (2003).
- [6] S. V. Shulga, S.-L. Drechsler, G. Fuchs, K.-H. Müller, K. Winzer, M. Heinecke, and K. Krug, *Phys. Rev. Lett.* **80**, 1730 (1998).
- [7] Y. Nakajima, T. Nakagawa, T. Tamegai, and H. Harima, *Phys. Rev. Lett.* **100**, 157001 (2008).
- [8] R. Gordon, M. D. Vannette, C. Martin, Y. Nakajima, T. Tamegai, and R. Prozorov, *Phys. Rev. B* **78**, 024514 (2008).
- [9] Y. Maeno, T. M. Rice, and M. Sigrist, *Phys. Today* **54**, 42 (2001) and references therein.
- [10] V. Z. Kresin and S. A. Wolf, *Physica C* **169**, 476 (1990).
- [11] R. A. Fisher, G. Li, J. C. Lashley, F. Bouquet, N. E. Phillips, D. G. Hinks, J. D. Jorgensen, and G. W. Crabtree, *Physica C* **385**, 180 (2003).
- [12] F. Manzano, A. Carrington, N. E. Hussey, S. Lee, A. Yamamoto, and S. Tajima, *Phys. Rev. Lett.* **88**, 047002 (2002).
- [13] J. Nagamastu, N. Nakagawa, T. Muranaka, Y. Zenitani, and J. Akimitsu, *Nature* **410**, 63 (2001).
- [14] Y. Singh, A. Niazi, M. D. Vannette, R. Prozorov, and D. C. Johnston *Phys. Rev. B* **76**, 214510 (2007).
- [15] J. M. Vandenberg, B. T. Matthias, E. Corenzwit, and H. Barz, *Mater. Res. Bull.* **10**, 889 (1975).
- [16] R. H. Blessing, *Acta Cryst.* **A51**, 33 (1995).
- [17] All software and sources of the scattering factors are contained in the SHELXTL (version 5.1) program library (G. Sheldrick, Bruker Analytical X-Ray Systems, Madison, WI).
- [18] For a topical review, see R. Prozorov and R. W. Gianetta, *Supercond. Sci. Technol.* **19**, R41 (2006).
- [19] Rietveld analysis program DBWS-9807a release 27.02.99, ©1998 by R. A. Young, an upgrade of “DBWS-9411 - an upgrade of the DBWS programs for Rietveld refinement with PC and mainframe computers, R. A. Young, *J. Appl. Cryst.* **28**, 366 (1995).”
- [20] R. B. Roof, Jr. and C. P. Kempter, *J. Chem. Phys.* **37**, 1473 (1962).
- [21] M. Hebbache, *Phys. Stat. Sol. RRL* **3**, 163 (2009). We thought that we were collaborating with this author on our present paper. Therefore it was a surprise to us when we saw his published paper. As the only author of his paper, Hebbache published our data (our Fig. 15 here) in his Fig. 1 and our SdH frequencies (Table III) in his Table 1 without our knowledge or consent. Furthermore, in his Ref. [4], he only acknowledged as a “private communication” two of the four authors of the present paper for the experimental data.
- [22] C. Kittel, *Solid State Physics*, 4th edition (John Wiley and Sons, New York, 1966).
- [23] M. Hebbache, L. Stuparević, and D. Živković, *Solid State Commun.* **139**, 227 (2006).
- [24] W. L. McMillan, *Phys. Rev.* **167**, 331 (1967).
- [25] T. ShibaYama, M. Nohara, H. A. Katori, Y. Okamoto, Z. Hiroi, and H. Takagi, *J. Phys. Soc. Jpn.* **76**, 073708 (2007).
- [26] K. Wakui, S. Akutagawa, N. Kase, K. Kawashima, T. Muranaka, Y. Iwahori, J. Abe, and J. Akimitsu, *J. Phys. Soc. Jpn.* **78**, 034710 (2009).
- [27] Y. Wang, R. Lortz, Y. Paderno, V. Filippov, S. Abe, U. Tutsch, and A. Junod, *Phys. Rev. B* **72**, 024548 (2005).
- [28] H. G. Smith and J. O. Wilhelm, *Rev. Mod. Phys.* **7**, 237 (1935).
- [29] N. R. Werthamer, E. Helfand, and P. C. Hohenberg, *Phys. Rev.* **147**, 295 (1966).
- [30] M. Tinkham, *Introduction to Superconductivity* (McGraw-Hill, New York, 1975).
- [31] L. M. Lifshitz and A. M. Kosevich, *Sov. Phys. JETP* **2**, 636 (1956).
- [32] D. Shoenberg, *Magnetic Oscillations in Metals* (Cambridge University Press, Cambridge and New York, 1984).
- [33] *Superconductivity*, Vol. 1, edited by R. D. Parks, (Marcel Dekker, New York, 1969).
- [34] V. G. Kogan, C. Martin, and R. Prozorov, *Phys. Rev. B* **80**, 014507 (2009).